

Properties of suspended graphene membranes

Graphene, a single layer of graphite, is a unique two-dimensional electron system as well as nature's thinnest elastic membrane. Here we review and describe our work on suspended graphene devices, focusing on their extraordinary mechanical, thermal, and electronic properties. These membranes bridge the traditional divide between "soft" and "hard" condensed matter physics, and have emerged as the ultimate platforms for exploring thin film mechanics, wrinkling instability, thermal transport, and electron scattering and correlations.

Chun Ning Lau*, Wenzhong Bao, and Jairo Velasco Jr.

Department of Physics and Astronomy, University of California, Riverside, Riverside, CA 92521, USA

*E-mail: jeaniel@ucr.edu

Graphene is a single layer of graphite, one atomic layer of carbon arranged in a honeycomb lattice (Fig. 1a). Since its experimental isolation on Si/SiO₂ substrates in 2004¹ and the experimental observation of the anomalous "half-integer" quantum Hall effect^{2,3}, graphene has taken both the scientific and technological communities by storm. It has become an extra-ordinary 2D electron system (2DES) for many-body phenomena and low dimensional physics, as well as a promising post-silicon electron material⁴⁻⁶.

The tremendous interest in graphene arises from its unique band structure, which consists of "cones" located at the two inequivalent Brillouin zone corners, where the conduction and valence bands touch at single points, or the so-called Dirac points (Fig. 1b). In the vicinity of the Dirac points, the energy-momentum dispersion relation is not governed by Schrödinger's equation, but rather by Dirac's equation for zero-rest mass particles, $E(k) = \hbar v_F k$, with an effective "speed of light" v_F , where $v_F \sim 10^6$ m/s is the Fermi velocity. This unique band structure endows graphene with extremely high mobility, unparalleled thermal conductivity, 98 % optical transparency and extraordinary current-carrying capacity – all of which are characteristics much sought-after in the electronics industry.

Scientifically, apart from its linear dispersion relation, graphene is distinct in several ways from traditional 2D electron systems (2DES) based on GaAs or Si: (1) graphene is truly 2D, being precisely one atomic layer; (2) its two inequivalent Dirac points lead to a novel quantum index, pseudo-spin, which is analogous to the "handedness" of neutrinos and gives rise to many novel phenomena such as the "half-integer" quantum Hall effect^{2,3}, Klein tunneling⁷⁻¹⁰ and suppression of back scattering¹¹; (3) graphene is a surface 2DES, enabling experiments that cannot be otherwise performed, such as optical spectroscopy, scanning tunneling microscopy (STM) and mechanical manipulation.

The earliest experiments on graphene were performed on devices on Si/SiO₂ substrates. However, substrates introduce scatterers, dopants and corrugations that obscure graphene's intrinsic electronic properties. Once suspended, these single- or few-atomic-layer membranes not only reveal their intrinsic transport properties, but also enable mechanical or optical transparency experiments that are traditionally not associated with 2DES, and generated one surprise after another. For instance, its mobility increases by more than two orders of magnitude^{12,13}; it is stronger than steel¹⁴ but suppler than Saran wrap^{15,16}; it is transparent

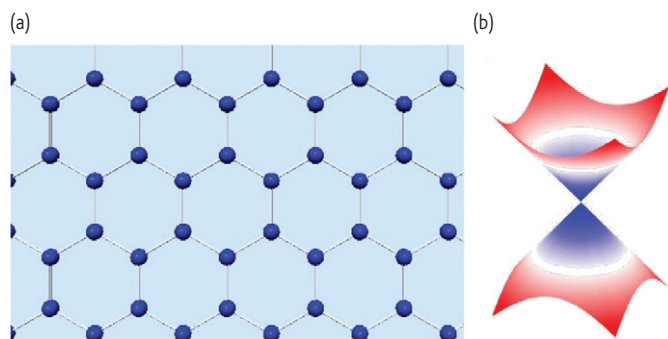


Fig. 1 (a) Lattice and (b) band structure of graphene.

yet very conductive^{17,18}; it conducts heat better than any other material. Thus, suspended graphene membranes have become the ultimate platform for exploring a wide variety of topics ranging from thin film mechanics^{16,19–24}, heat transport^{25–35}, and electronic correlations^{36–45}.

Fabrication

Fabricating free-standing graphene devices is no easy feat, since these single atomic layer membranes are exceedingly fragile to handle, while the device geometry becomes ever more complex. For instance, transport studies often require devices with top gates, which, together with back gates, allow independent tuning of charge density and out-of-plane electric field. In our laboratory we have developed two different methods to fabricate suspended graphene devices with and without top gates.

In the first and more conventional technique, electrodes are deposited on graphene sheets on Si/SiO₂ substrates via standard electron-beam lithography. If desired, a multi-level lithography technique is employed

to fabricate Cr top gates that are suspended ~100 – 300 nm above graphene^{46,47}. The completed devices are immersed in hydrofluoric acid that partially removes the underlying SiO₂ layer, then dried in a critical point dryer^{12,13}. These devices that undergo lithographical wet processes typically have linear dimensions limited to 1 – 2 μm, and mobility ranging from 20 000 to 150 000 cm²/Vs at low temperature. For comparison, the low temperature mobility values of devices on Si/SiO₂ substrates are typically lower by an order of magnitude, ~2000 to 15 000 cm²/Vs. Scanning electron micrograph (SEM) images of singly- and dual-gated devices are shown in Fig. 2a,b.

Lithographical processes are known to introduce surface or chemical contaminants, such as resist residues, which significantly reduce device mobility. To fabricate ultra-clean graphene devices, we developed a lithography-free technique⁴⁸. Here graphene sheets are exfoliated across the trenches, and coupled to electrodes by evaporating metals through carefully aligned silicon shadow masks (Fig. 2c). Realization of a double-gated geometry in these type of devices is achieved by simply (but delicately) laying down a second piece of Si/SiO₂ chip, which covers the entire suspended device and acts as the top gate. Our transport and STM measurements verified that these lithography-free devices are exceedingly clean, with no chemical residue and little adsorbates, and mobility values up to 250 000 cm²/Vs for single layer graphene at $T = 1.5$ K⁴⁸.

Electrical properties

Mobility and annealing

The most basic electrical property of graphene is its bipolar field effect transistor (FET) behavior, where a nearby electrostatic gate (usually provided by the heavily doped Si substrate) is used to tune the density and polarity of

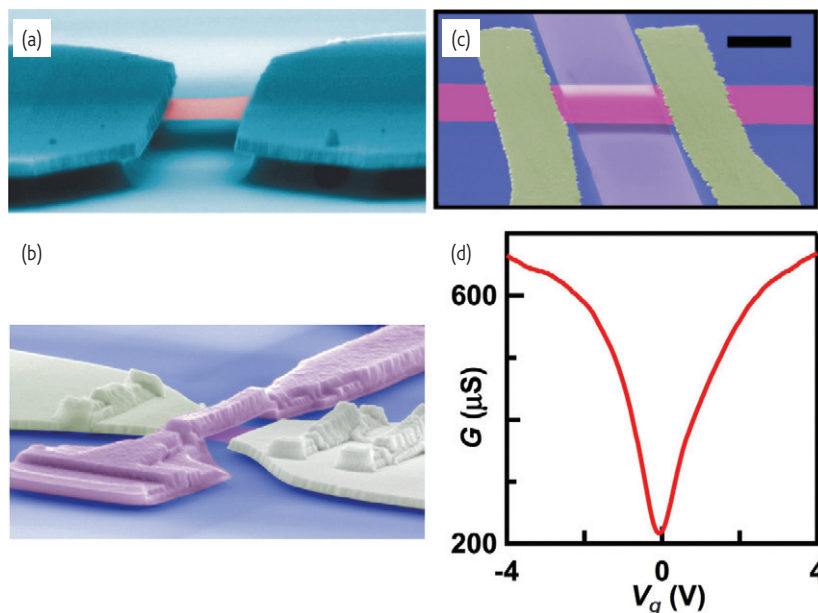


Fig. 2 (a,b) SEM images of singly- and dual-gate graphene fabricated via acid etching of SiO₂ layer. (b) is reprinted with permission from⁶⁷. (c) SEM image of a graphene device fabricated using the lithography-free technique. Scale bar: 2 μm. (d) Conductance vs gate voltage of a suspended BLG device, with mobility ~40 000 cm²/Vs.

charge carriers in graphene, thereby modulating its conductance. For devices on Si substrates with 300 nm of SiO₂, 1 V in gate voltage V_g induces charge density $n \sim 7.2 \times 10^{14} \text{ m}^{-2}$; for typical suspended devices, the n/V_g ratio is $\sim 2 \times 10^{14} - 4 \times 10^{14} \text{ m}^{-2}\text{V}^{-1}$. Fig. 2d displays the standard curve of device conductivity σ vs. V_g , which is V-shaped, with a finite minimum conductivity value σ_{min} at the charge neutrality point (CNP), where graphene is undoped with nominally zero charge. Graphene is hole- or p -doped at $V_g < V_{g,\text{min}}$ and electron- or n -doped at $V_g > V_{g,\text{min}}$. Away from the CNP, σ increases approximately linearly with V_g ; the slope of the $\sigma(V_g)$ curve yields the field effect mobility, $\mu = (1/e) d\sigma/dn$, that characterizes the device quality. Here e is electron charge and n is charge density. As mentioned above, μ ranges from 2000 – 15 000 cm²/Vs for devices supported on Si/SiO₂ substrates, which are generally considered mobility bottlenecks, as they introduce scatterings from surface phonons, charge puddles that arise from charged impurities and/or corrugations, and other neutral impurities.

By eliminating substrates, mobility of graphene devices increases dramatically, with a mean free path as large as 1 μm ¹³. One caveat is that this is only achieved after a crucial current annealing step⁴⁹, since mobility of as-fabricated suspended graphene devices is limited by adsorbates and/or resist residues. We find that the optimal annealing is typically achieved at $\sim 0.2 \text{ mA}/\mu\text{m}/\text{layer}$ at low temperature $T = 4 \text{ K}$ ⁵⁰. The temperature at the center of the device is estimated to be $\sim PL/8aK$, where P is the Joule power, L is the length, a is the cross-sectional area, and K is the thermal conductivity of graphene. Using $K \sim 600 \text{ W/mK}$ (see section below), we estimate that the center of graphene is annealed to $\sim 500 \text{ K}$, which is hot enough to desorb the resist residues and volatile adsorbates. After annealing, device mobility at 4 K reaches 250 000 cm²/Vs for single layer graphene (SLG)¹³, and 350 000 – 500 000 for bilayer (BLG) and trilayer graphene (TLG) devices^{50–53}.

Another insight into suspended graphene can be seen in the expression for r_s , the electronic interaction strength, which is approximately the ratio of the inter-electron Coulomb energy to the Fermi energy. In graphene, $r_s \propto n^{-(p-1)/2} / \epsilon_r$, where ϵ_r is the dielectric constant of the environment and p is the power of the dispersion relation. Thus interaction-driven phenomena are more easily accessed at low density and in suspended graphene with $\epsilon_r = 1$. Interestingly, compared to SLG, r_s is much larger in its few layer counterparts, since $p = 1, 2$, and 3 for SLG, BLG, and rhombohedral-stacked TLG (see below), respectively⁶. Thus BLG and TLG afford fascinating many-body physics, and in the rest of this section we will focus on our experiments in these systems.

Suspended bilayer graphene

In a Bernal-stacked (or AB-stacked) BLG, atoms of one sub-lattice in the top layer are located above the centers of the hexagons of the bottom layer (Fig. 3a). BLG's charge carriers behave as massive Dirac fermions, with low energy bands given by^{54–56} $E = \pm \hbar^2 k^2 / 2m^*$, where $m^* \sim 0.03m_e$ is the effective mass of charge carriers and m_e is electron rest mass (Fig. 3b). Like SLG, charges in BLG are also chiral, with layer, sublattice and spin degrees of freedom. When an external potential V_{\perp} is applied across the bilayer, the band structure adopts a “Mexican-hat” shape, with a band gap (Fig. 3c)

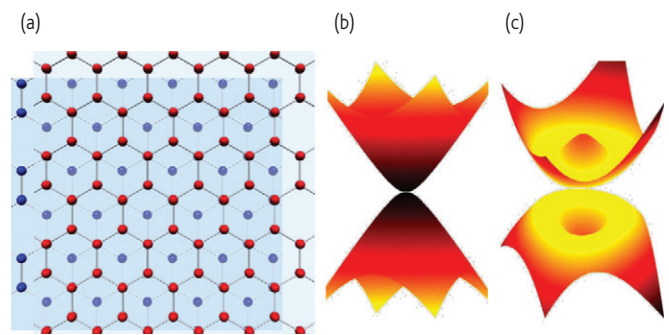


Fig. 3 (a) BLG schematic. Atoms in the top and bottom layers are shown in red and blue, respectively. (b,c) Band structures of BLG in zero and finite E_{\perp} , respectively.

$$\Delta = \frac{t_{\perp} V_{\perp}}{\sqrt{t_{\perp}^2 + V_{\perp}^2}} \quad (1)$$

where $t_{\perp} \sim 0.2 - 0.4 \text{ eV}$ is the interlayer hopping energy. This opening of a band gap that is controlled by an external electric field has generated significant interest as a promising route to band gap engineering in graphene electronics^{56–64}.

In our dual-gated suspended BLG devices, we can independently adjust the total charge density n and the applied electric field $E_{\perp} = V_{\perp} / d$ that breaks the inversion symmetry, where $d = 3.34 \text{ \AA}$ is the interlayer spacing,

$$E_{\perp} = (n_{\text{bg}} - n_{\text{tg}}) \frac{e}{2\epsilon_0} \quad \text{and} \quad n = n_{\text{bg}} + n_{\text{tg}}, \quad (2)$$

where $n_{\text{bg}} = (C_{\text{bg}}/e)V_{\text{bg}}$, $n_{\text{tg}} = (C_{\text{tg}}/e)V_{\text{tg}}$, and C_{bg} and C_{tg} are capacitance per unit area between graphene and the gates. Data sets from two typical BLG devices are shown in Fig. 4.

Fig. 4a plots the data set from device 1, which has mobility $\sim 20\,000 \text{ cm}^2/\text{Vs}$. In the upper panel that plots device conductance G (color) as functions of E_{\perp} (vertical axis) and n (horizontal axis), the vertical feature at $n = 0$ reflects the change in minimum conductivity with E_{\perp} . Line traces $G(n)$ at different E_{\perp} are shown in the lower panel. Clearly, σ_{min} exhibits a maximum at $E_{\perp} = 0$ and monotonically decreases with increasing E_{\perp} of either polarity. Such behavior is expected from single particle calculations, since, from Eq. (1), the induced gap grows with E_{\perp} and results in monotonically decreasing conductance at the CNP.

In contrast, device 2, which has a mobility of $80\,000 \text{ cm}^2/\text{Vs}$, displays a markedly different behavior (Fig. 4b) – namely a conductance *minimum* appears at $n = E_{\perp} = 0$. In fact, this device is *insulating* at the CNP in the absence of any applied E_{\perp} , with conductance as low as $< 0.5 \mu\text{S}$. This is further elucidated by the differential conductance curve dI/dV vs. source-drain bias V , which displays sharp peaks at $\sim \pm 2 \text{ mV}$ that strongly resembles the density of states of a gapped state (Fig. 4c,d). This gapped state can be closed by applying E_{\perp} of either polarity – with increasing $|E_{\perp}|$ up to $\sim 15 \text{ mV/nm}$, the sharp peaks in dI/dV disappear and the conductance increases to $\sim 300 \mu\text{S}$ (Fig. 4d). Upon further increase in $|E_{\perp}|$, G decreases again, reverting to the single particle behavior of gap opening induced by interlayer potential bias.

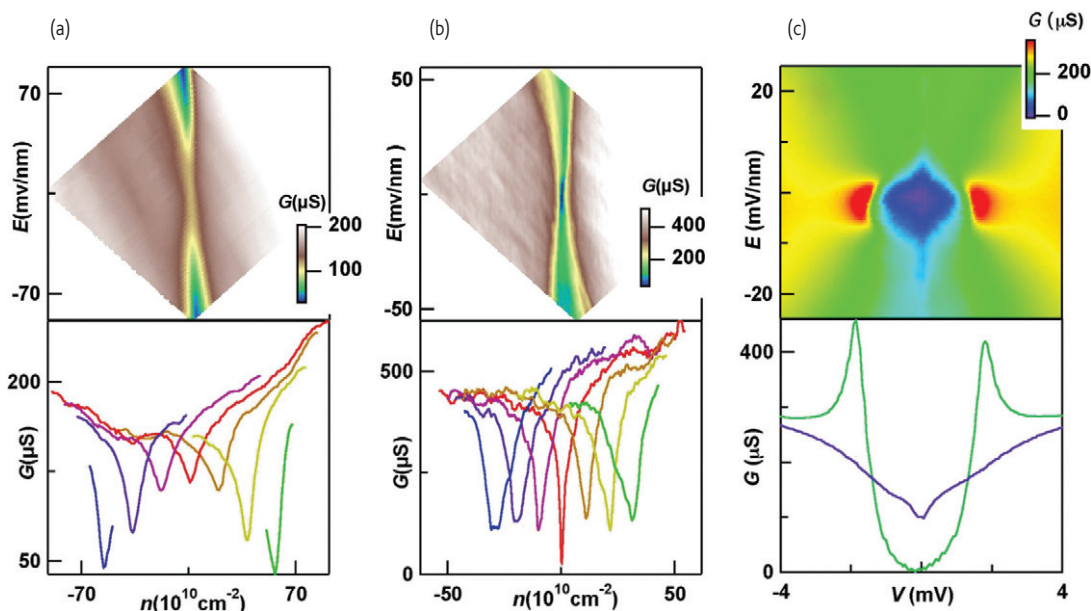


Fig. 4 (a) (Upper panel) Conductance G vs. n and E_{\perp} for a device with mobility $\sim 20\,000\text{ cm}^2/\text{Vs}$. (Lower panel) Line traces $G(n)$ at $E_{\perp} = -81, -54, -27, 0, 27, 54$ and 81 mV/nm (left to right). (b) Similar data set for a device with high mobility $\sim 80\,000\text{ cm}^2/\text{Vs}$. The line traces are taken at $E_{\perp} = -37.5, -25, -12.5, 0, 12.5, 25$ and 37.5 mV/nm (left to right). (c) dI/dV vs. source-drain bias V and E_{\perp} . (d) Line traces $dI/dV(V)$ at $E_{\perp} = 0$ (green) and -12.5 mV/nm (purple). Adapted and reprinted with permission from⁶⁷.

The insulating state at $n=E_{\perp}=0$ is an example of interaction-driven physics expected in BLG, which, because of the flat bands near the CNP, are predicted to host ordered state(s) with spontaneously broken symmetries^{36-45,65}. Such states, according to various theoretical proposals, are: a gapped anomalous Hall state^{39,42,66} or a current loop state⁴⁵ with broken time-reversal symmetry, a gapped antiferromagnet state with broken time reversal and spin rotation symmetry^{42-44,65,67}, a gapless nematic state which breaks in-plane rotational symmetry^{40,41}. Recent experiments^{53,66-69} have provided signatures of these states, and our results are most consistent with either the antiferromagnet state or the current loop state. Nevertheless, the exact nature of the ground state and possible transition among the various phases remain fascinating theoretical and experimental challenges.

Suspended trilayer graphene

BLG only has one stable configuration of Bernal stacking. In contrast, TLG has two natural stable allotropes, Bernal and rhombohedral stacking orders, distinguished only by the relative position of the *topmost* and the *bottom* layers – they can be either AA stacked, yielding ABA- or Bernal-stacked TLG (B-TLG), or AB stacked, yielding ABC- or rhombohedral-stacked TLG (r-TLG) (Fig. 5a-b insets). Their band structures are dramatically different: the dispersion of B-TLG is a combination of the linear dispersion of SLG and the quadratic relation of BLG (Fig. 5a), whereas for r-TLG, $E(k) \sim k^3$ (Fig. 5b)⁷⁰⁻⁷². These distinctive band structures are expected to give rise to different transport and optical properties⁷³⁻⁷⁶. For instance, under an applied electric field, B-TLG is expected to have band overlap whereas r-TLG is predicted to open a band gap^{69-72,77-81}, similar to that observed in bilayer graphene.

To investigate the intrinsic electrical properties of TLG, we use the lithography-free technique to fabricate a large number of suspended TLG devices, and study their behaviors at $T = 1.5\text{ K}$. All devices are conductive at large n . The real surprise comes at low n : r-TLG devices become insulating ($G \sim 0.1\ \mu\text{S}$) at the CNP, whereas B-TLG remains conductive ($G \sim 100\ \mu\text{S}$). Thus, even the seemingly minute difference in stacking gives rise to dramatically different transport properties (Fig. 5c)⁵⁰.

Our temperature dependence and dI/dV measurements (Fig. 5d-e) of r-TLG at the CNP reveal an activation gap of $\sim 6\text{ meV}$, which is even larger than the gap measured in BLG. This insulating state in r-TLG, like that in BLG, cannot be explained by the single particle picture. However, it is consistent with the fact that r-TLG is even more susceptible to electronic interactions, because of the very flat bands near the CNP and significantly enhanced interaction strength r_s ⁴². Thus, our demonstration of the insulating state in r-TLG is a first indication of such interaction-driven physics, and underscores the rich many-body phenomena that are possible in this system.

More generally, we now know that few layer graphene with different stacking orders can have dramatically different behaviors, from gapped insulators to metallic conductors. But there is no reason to stop at TLG. For instance, an N -layer graphene sheet can have up to 2^{N-2} stacking orders. Thus, stacking order of the layers provides another possible route for controlling the electronic properties of FLG systems.

Thermal properties

Thermal expansion

Most materials have positive thermal expansion coefficient (TEC), *i.e.* they expand when heated, and contract when cooled. The exceptions

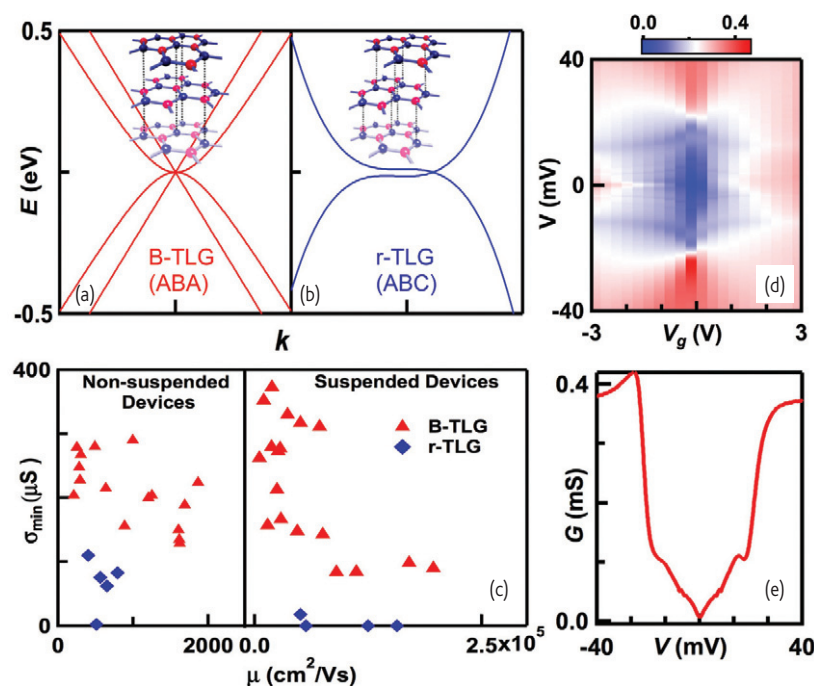


Fig. 5 (a,b) Band structures (main panel) and schematics (inset) of ABA- and ABC-stacked TLG, respectively. (c) Minimum conductivity σ_{min} vs. field effect mobility μ at 4 K for suspended and non-suspended graphene devices. (d) $dI/dV(V_g, V)$ for an r-TLG at $B = 0$ and $T = 300$ mK. (e) Line trace of (d) at $V_g = 0$. Adapted and reprinted with permission from⁵⁰.

to the rule are membranes, which often have negative TEC. This curious phenomenon arises from the very soft ZA (out-of-plane acoustic) phonon mode in the 2D membranes, which, contrary to acoustic phonons in most materials, increases in frequency when inter-atomic spacing is increased. Such “membrane effect”, first predicted by Lifshitz in 1952⁸², manifests as negative in-plane TEC in many layered compounds, including graphite.

Though graphene was predicted to exhibit negative in-plane TEC at room temperature^{24,83}, experimental determination of graphene’s TEC is very challenging. Traditional techniques of TEC measurements, such as x-ray or neutron diffraction, strain gauges, dilatometers and optical interferometry⁸⁴, are designed for bulk materials, and cannot be applied for atomic membranes. Thus we developed an unconventional technique by heating and cooling suspended graphene membranes while monitoring their morphology change via *in situ* SEM imaging¹⁶. During the cooling process, due to the negative TEC, graphene expand but its edges are pinned by the substrates, thus it buckles and sags during the cooling process. We measure the ratio $l(T) = L_g(T)/L_t(T)$, where L_g is the length of graphene membrane’s edge as measured along the arc, and L_t is the length of the trench measured along the chord (Fig. 6a). Since the membrane’s vertical displacement $\zeta \propto L_t \sqrt{l-1}$, even a miniscule deviation of l from unity produces notable changes in ζ that are readily detected in the SEM images.

In Fig. 6b we plot $l(T)$ for a SLG sheet. The slope of the graph dl/dT then yields the difference in TEC between graphene and the substrate. The measured $\alpha_{graphene}$ results are shown as the blue lines in Fig. 6. At 300K, $\alpha_{graphene} \sim -7 \times 10^{-6} K^{-1}$, which is much larger than graphite’s

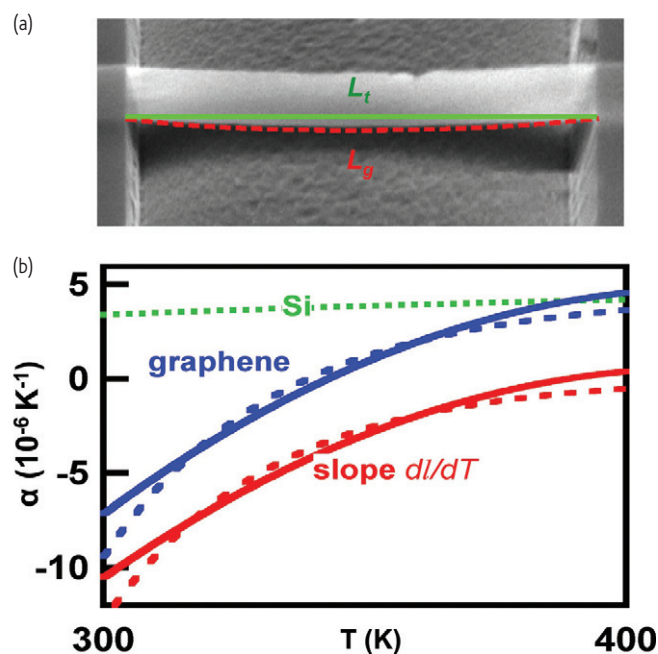


Fig. 6 (a) SEM image of a graphene device that sags during the cooling process. Scale bar: 1 μm . (b) Thermal expansion coefficient of graphene (blue) as function of temperature. The solid and dotted lines correspond to value obtained with different fitting procedures. Adapted and reprinted with permission from¹⁶.

in-plane TEC, $\sim -1 \times 10^{-6} K^{-1}$, and 2 – 3 times larger than theoretical predictions. This anomalously large and negative TEC value should be an interesting venue for further experimental and theoretical investigations.

We note that our measurements represent a lower bound for $|\alpha|$, since we assume no sliding between the substrate and graphene during the cooling process. More recently, other unconventional techniques were applied to measure graphene's TEC, by measuring thermally induced strain using Raman spectroscopy or electromechanical resonance⁸⁵⁻⁸⁷. These measurements verified the large TEC at room temperature, and that it remains negative for a large temperature range 30 – 400 K. Another important question is graphene's TEC at high temperatures, which has been predicted to either stay negative⁸³ or become positive due to quantum mechanical effects²⁴, thus calling for further experimental investigation.

Such large, negative TEC of graphene has important implications on graphene electronics, since the TEC differential at the interface of different materials is the most common mechanism underlying thermally induced stress, cracks and device failure. Thus, it is crucial to take the negative TEC of graphene into account during device engineering for large-scale integration of graphene devices.

Thermal conductivity

Suspended graphene has very high thermal conductivity. Because of the strong C-C bond and high phonon speed ($\sim 2 \times 10^4$ m/s), thermal conductivity K of graphene at room temperature is dominated by phonon contribution. In the first measurement of K ²⁶, a laser from a Raman spectrometer is used to induce a temperature rise that is in turn estimated by the position of the G peak of the Raman spectrum at 1580 cm^{-1} . This G peak arises from the doubly degenerate in-plane optical phonons of E_{2g} symmetry, and, due to the anharmonicity of the graphene lattice, downshifts in frequency with increasing temperature²⁵. Using this optothermal technique, the "three-dimensional" thermal conductivity of graphene (assuming an effective thickness of $d = 3.34 \text{ \AA}$) is determined to be $\sim 2000 - 5000 \text{ W/mK}$ near or above room temperature³²⁻³⁴, $\sim 600 \text{ W/mK}$ at $\sim 600\text{K}$ ³⁵. For comparison, K is $\sim 400 \text{ W/mK}$ for copper and ~ 150 for silicon at room temperature. When graphene is supported on substrates, K decreases to $\sim 600 \text{ W/mK}$ ²⁹ due to phonon leakage to substrates, as well as scattering of phonon off defects and corrugations induced by the substrates. This lower K value still compares favorably with Cu and Si. Thus graphene is a very attractive material for thermal management, e.g. as heat spreaders, for the electronics industry.

Mechanical Properties – a new wrinkle

Since its discovery, graphene has often been dubbed "carbon flatland" and depicted as a plane of very rigid "chicken wires" that remains perfectly flat. Such portrayal, together with graphene's amazing electronic properties, eclipses the fact that it is also nature's thinnest elastic membrane with exceptional mechanical properties. Suspended graphene sheets have been demonstrated to display random ripples at room temperature⁸⁸, or act as sensitive nano-electromechanical (NEM) resonators⁸⁹⁻⁹¹ and impermeable membranes⁹² with extremely high elastic constant⁹³ and strength¹⁴.

Our venture into this area begins when we suspend graphene membranes of 1 – 50 layers by exfoliating across pre-defined trenches on Si/SiO₂ substrates. Much to our surprise, most of the graphene membranes are not flat, but form periodic ripples. These *static* ripples can be imaged in tilted stage in an SEM, using tapping mode in atomic force microscope (AFM), or even under optical microscope for thicker films (Fig. 7a-c)¹⁶.

Upon closer inspection using AFM, the ripples have almost perfectly sinusoidal profile, with out-of plane displacement ζ described by $\zeta = A \sin(2\pi y/\lambda)$, where A is the amplitude and λ the wavelength. They can be induced by either transverse compression in the y direction, or by longitudinal strain and/or shear in the x -direction. These ripples are analogous to those found in thin films, and arise from a competition between bending and stretching⁹⁴; since the bending rigidity of graphene is extremely small (for thin films, in the continuum approximation, the bending rigidity scales with Yt^3 , where Y is the Young's modulus and t is the thickness of the membrane), graphene deforms readily to form ripples under tiny tensile strain.

From classical elasticity theory, we expect that the ripple parameters, including A , λ , length L , thickness of membrane t and Poisson ratio ν are related by the following equations,

$$\frac{A\lambda}{L} = \sqrt{\frac{8\nu}{3(1-\nu^2)}}t \quad (3a)$$

$$\text{and} \quad \frac{A\lambda}{L} = \sqrt{\frac{8}{3(1+\nu)}}t \quad (3b)$$

for membranes under longitudinal strain and shear, respectively. Using values of A , L , λ and t as determined from AFM imaging, and $\nu = 0.165$ for graphite in the basal plane, $A\lambda/L$ vs. t is plotted for 51 samples that display periodic ripples (Fig. 7d). Eqs. (3a) and (3b) are plotted as the lower and upper solid lines, respectively. Most data points fall on the lower line, indicating that ripples in them are induced by pre-existing longitudinal strains. The six data points that fall above the upper line suggest the presence of shear in those samples.

The tensile strains γ in these atomic membranes, while difficult to determine using conventional techniques, can be readily obtained by

$$\gamma = \frac{4(\pi t L)^2}{3(1-\nu^2)\lambda^4} \quad (4)$$

for strain-induced ripples⁹⁴. For our suspended devices, γ ranges from $\sim 0.016\% - 0.3\%$ in thicker films, to as large as 1.5% in SLG and BLG (Fig. 7e).

To generate compressive strains, we take advantage of graphene's negative TEC and thermally cycle the devices. With increasing temperature T , the large mismatch between the TEC of graphene and the substrate puts the former in biaxial tension. Conversely, upon decreasing T , graphene expands and, as its edges are pinned by the trench edges, is under compressive strain. Because of its extremely small bending

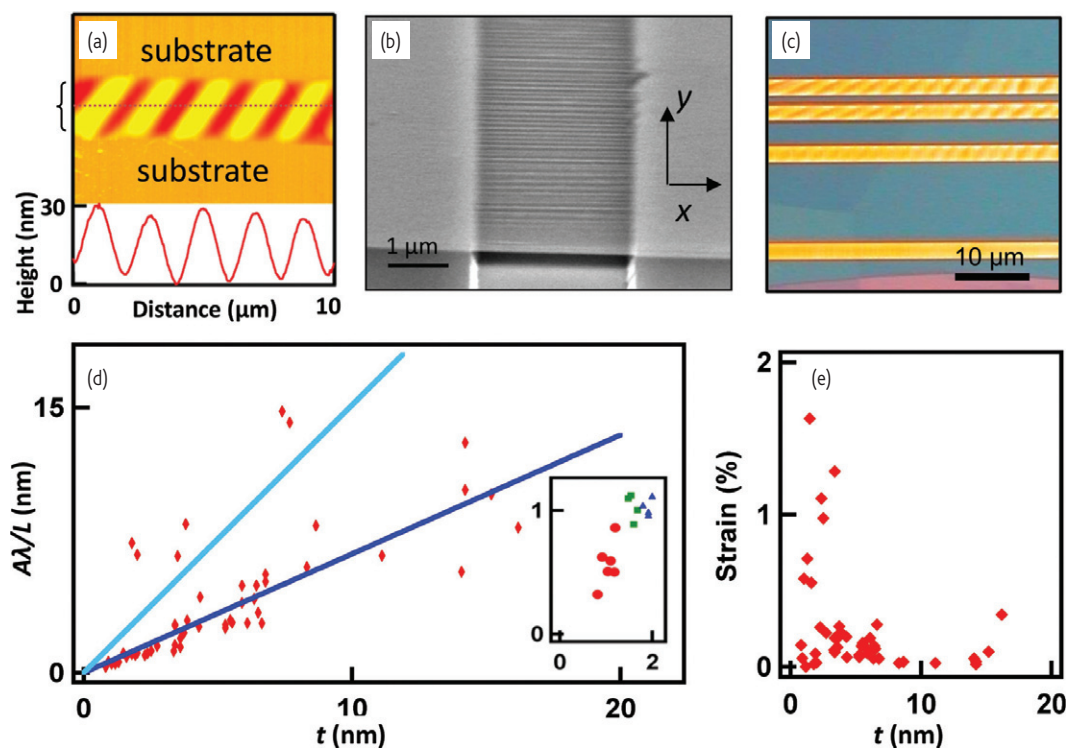



Fig. 7 Images, morphology and strain of suspended graphene sheets. (a) Data from a graphene membranes suspended across trenches. The center horizontal stripe, indicated by the left bracket in (a), corresponds to the trench. Upper panels: AFM topographical images. Lower panels: line traces taken along the dotted lines. Note the different amplitudes and wavelengths of the devices. (b) SEM image of a bi-layer suspended membrane. (c) Optical image of a thicker graphene sheet with ripples. (d) $A\lambda/L$ vs t for 51 membrane devices. The lower and upper lines are calculated using $\nu = 0.165$ and Eqs. (3) and (4), respectively. Inset: $A\lambda/L$ vs. t for single (red)-, bi (green)- and triple (blue)- layer devices. The number of layers is inferred from color contrast in optical microscope, though only measured thickness is used. (e) Strain in suspended devices, calculated using Eq. (4). Adapted and reprinted with permission from¹⁶.

rigidity, the strain is accommodated by out-of-plane deformations, thus producing buckles in the x direction and ripples in the y direction. Since the compressive strain arises from the difference in TEC between the substrate and graphene, the amplitude of the ripples $A \sim \lambda\sqrt{\gamma} \sim \lambda\sqrt{\Delta T}$, where ΔT is the change in temperature. This is indeed borne out by experimental data¹⁶.

The above experiments demonstrated the membrane nature of graphene. More recently, there is growing interest in understanding wrinkling and crumpling instability in graphene¹⁹⁻²³. For instance, the wrinkle formation in graphene can be accounted for by the “wrinklon” theory²³. A wrinklon describes a localization transition region in which two wrinkles merge, resulting from boundary confinement and gives rise to a universal self-similar hierarchy of wrinkles. This theory is validated for thin films with thickness spanning 6 – 7 orders of magnitude, ranging from atomic graphene membranes to large window curtains. Thus graphene, with its atomic thickness and unparalleled aspect ratio, has become the ultimate thin film to explore membrane physics and mechanics.

Conclusion

Graphene is truly a unique material, with the double identity as both an elastic membrane and an electron system. Suspended devices have

enabled many of the most revealing experiments on graphene to date, from its membrane-like suppleness and elasticity, optical transparency, to its fantastic mobility, thermal conductivity and accessibility of interaction phenomena. Free-standing graphene should continue to yield insights into this electronic and optical membrane. A unique and particularly attractive direction is the interplay between the “hard” and “soft” aspects of graphene. For instance, ripples and strains in graphene are more than just mechanical curiosity, since the local electronic properties of graphene is intricately related to its local morphology: strain changes the momentum of charge carriers, thereby creating both scalar and vector potentials; spatial or temporal variations of these potentials may thus create effective electric and magnetic fields. Various theoretical proposals suggest fantastic possibilities such as electron super-collimators^{95,96}, anisotropic transport⁹⁷, modification of band structures⁹⁸, and generation of effective magnetic field^{99,100}. Realization of such “strain-tronics” in transport studies represents an interesting and promising challenge. Other possibilities include triggering quantum phase transitions among the ordered states in BLG via strain, and using curvatures to induce selective functionalization and create superlattices. Thus, uniting the traditional division of “hard” and “soft” condensed matter physics, many novel phenomena await in this electronic membrane. 

Acknowledgement

The authors acknowledge the support by NSF CAREER DMR/0748910, NSF DMR/1106358, NSF CBET/0756359, ONR N00014-09-1-0724,

ONR/DMEA H94003-10-2-1003 and the FENA Focus Center. CNL acknowledges the support by the "Physics of Graphene" program at KITP.

REFERENCES

1. Novoselov, K. S., *et al.*, *Science* (2004) **306**, 666.
2. Novoselov, K. S., *et al.*, *Nature* (2005) **438**, 197.
3. Zhang, Y. B., *et al.*, *Nature* (2005) **438**, 201.
4. Castro Neto, A. H., *et al.*, *Rev Mod Phys* (2009) **81**, 109.
5. Fuhrer, M. S., *et al.*, *MRS Bulletin* (2010) **35**, 289.
6. Das Sarma, S., *et al.*, *Rev Mod Phys* (2011) **83**, 407.
7. Cheianov, V. V., and Fal'ko, V. I., *Phys Rev B* (2006) **74**, 041403.
8. Katsnelson, M. I., *et al.*, *Nat Phys* (2006) **2**, 620.
9. Young, A. F., and Kim, P., *Nat Phys* (2009) **5**, 222.
10. Stander, N., *et al.*, *Phys Rev Lett* (2009) **102**, 026807.
11. McEuen, P. L., *et al.*, *Phys Rev Lett* (1999) **83**, 5098.
12. Bolotin, K. I., *et al.*, *Sol State Commun* (2008) **146**, 351.
13. Du, X., *et al.*, *Nat Nanotechnol* (2008) **3**, 491.
14. Lee, C., *et al.*, *Science* (2008) **321**, 385.
15. Poot, M., and van der Zant, H. S. J., *Appl Phys Lett* (2008) **92**, 063111.
16. Bao, W. Z., *et al.*, *Nat Nanotechnol* (2009) **4**, 562.
17. Mak, K. F., *et al.*, *Phys Rev Lett* (2008) **101**, 196405.
18. Nair, R. R., *et al.*, *Science* (2008) **320**, 1308.
19. Balankin, A. S., *et al.*, *Phys Rev E* (2011) **84**, 021118.
20. Min, K., and Aluru, N. R., *Appl Phys Lett* (2011) **98**, 013113.
21. Paronyan, T. M., *et al.*, *ACS Nano* (2011) **5**, 9619.
22. Pereira, V. M., *et al.*, *Phys Rev Lett* (2010) **105**, 156603.
23. Vandeparre, H., *et al.*, *Phys Rev Lett* (2011) **106**, 224301.
24. Zakharchenko, K. V., *et al.*, *Phys Rev Lett* (2009) **102**, 046808.
25. Calizo, I., *et al.*, *Nano Lett* (2007) **7**, 2645.
26. Balandin, A. A., *et al.*, *Nano Lett* (2008) **8**, 902.
27. Chen, Z., *et al.*, *Appl Phys Lett* (2009) **95**, 161910.
28. Jang, W., *et al.*, *Nano Lett* (2010) **10**, 3909.
29. Seol, J. H., *et al.*, *Science* (2010) **328**, 213.
30. Wei, P., *et al.*, *Phys Rev Lett* (2009) **102**, 166808.
31. Zuev, Y. M., *et al.*, *Phys Rev Lett* (2009) **102**, 096807.
32. Ghosh, S., *et al.*, *Nat Mater* (2010) **9**, 555.
33. Murali, R., *et al.*, *Appl Phys Lett* (2009) **94**.
34. Cai, W. W., *et al.*, *Nano Lett* (2010) **10**, 1645.
35. Faugeras, C., *et al.*, *ACS Nano* (2010) **4**, 1889.
36. Min, H., *et al.*, *Phys Rev B* (2008) **77**, 041407.
37. Castro, E. V., *et al.*, *Phys Rev Lett* (2008) **100**, 186803.
38. Martin, I., *et al.*, *Phys Rev Lett* (2008) **100**, 036804.
39. Nandkishore, R., and Levitov, L., *Phys Rev B* (2010) **82**, 115124.
40. Vafek, O., and Yang, K., *Phys Rev B* (2010) **81**, 041401.
41. Lemonik, Y., *et al.*, *Phys Rev B* (2010) **82**, 201408.
42. Zhang, F., *et al.*, *Phys Rev Lett* (2011) **106**, 156801.
43. Jung, J., *et al.*, *Phys Rev B* (2011) **83**, 115408.
44. Kharitonov, M., *preprint* (2011) arXiv:1105.5386v1.
45. Zhu, L., *et al.*, (2012) arXiv:1202.0821v1.
46. Liu, G., *et al.*, *Appl Phys Lett* (2008) **92**, 203103.
47. Velasco, J., *et al.*, *Phys Rev B* (2010) **81**, R121407.
48. Bao, W. Z., *et al.*, *Nano Res* (2010) **3**, 98.
49. Moser, J., *et al.*, *Appl Phys Lett* (2007) **91**, 163513.
50. Bao, W., *et al.*, *Nat Phys* (2011) **7**, 948.
51. Bao, W. Z., *et al.*, *Phys Rev Lett* (2010) **105**, 246601.
52. Bao, W., *et al.*, *Proc Natl Acad Sci U S A* (2012) to appear.
53. Mayorov, A. S., *et al.*, *Science* (2011) **333**, 860.
54. McCann, E., *Phys Rev B* (2006) **74**, 161403.
55. Novoselov, K. S., *et al.*, *Nat Phys* (2006) **2**, 177.
56. Castro, E. V., *et al.*, *Phys Rev Lett* (2007) **99**, 216802.
57. Oostinga, J. B., *et al.*, *Nat Mater* (2008) **7**, 151.
58. Kuzmenko, A. B., *et al.*, *Phys Rev B* (2009) 165406.
59. Mak, K. F., *et al.*, *Phys Rev Lett* (2009) **102**, 256405.
60. Zhang, Y. B., *et al.*, *Nature* (2009) **459**, 820.
61. Xia, F. N., *et al.*, *Nano Lett* (2010) **10**, 715.
62. Taychatanapat, T., and Jarrillo-Herrero, P., *Phys Rev Lett* (2010) **105**, 166601.
63. Zou, K., and Zhu, J., *Phys Rev B* (2010) 081407.
64. Jing, L., *et al.*, *Nano Lett* (2010) **10**, 4000.
65. Zhang, F., *et al.*, *Phys Rev B* (2010) **81**, 041402 (R).
66. Weitz, R. T., *et al.*, *Science* (2010) **330**, 812.
67. Velasco, J., *et al.*, *Nature Nanotechnol* (2012) **7**, 156.
68. Martin, J., *et al.*, *Phys Rev Lett* (2010) **105**, 256806.
69. Freitag, F., *et al.*, *Phys Rev Lett* (2012) **108**, 076602.
70. Guinea, F., *et al.*, *Phys Rev B* (2006) **73**, 245426.
71. Aoki, M., and Amawashi, H., *Sol State Commun* (2007) **142**, 123.
72. Zhang, F., *et al.*, *Phys Rev B* (2010) **82**, 035409.
73. Craciun, M. F., *et al.*, *Nat Nanotechnol* (2009) **4**, 383.
74. Lui, C. H., *et al.*, *Nat Phys* (2011) **7**, 944.
75. Taychatanapat, T., *et al.*, *Nat Phys* (2011) **7**, 621.
76. Zhang, L., *et al.*, *Nat Phys* (2011) **7**, 953.
77. Partoens, B., and Peeters, F. M., *Phys Rev B* (2006) **74**, 075404.
78. Latil, S., and Henrard, L., *Phys Rev Lett* (2006) **97**, 036803.
79. Koshino, M., and Ando, T., *Phys Rev B* (2007) **76**, 085425.
80. Manes, J. L., *et al.*, *Phys Rev B* (2007) **75**, 155424.
81. Avetisyan, A. A., *et al.*, *Phys Rev B* (2010) **81**, 115432.
82. Lifshitz, I. M., *Zh Eksp Teor Fiz* (1952) **22**, 475.
83. Mounet, N., and Marzari, N., *Phys Rev B* (2005) **71**, 205214.
84. James, J. D., *et al.*, *Meas Sci Technol* (2001) **12**, R1.
85. Chen, C.-C., *et al.*, *Nano Lett* (2009) **9**, 4172.
86. Singh, V., *et al.*, *Nanotechnol* (2010) **21**, 165204.
87. Yoon, D., *et al.*, *Nano Lett* (2011) **11**, 3227.
88. Meyer, J. C., *et al.*, *Nature* (2007) **446**, 60.
89. Bunch, J. S., *et al.*, *Science* (2007) **315**, 490.
90. Garcia-Sanchez, D., *et al.*, *Nano Lett* (2008) **8**, 1399.
91. Chen, C. Y., *et al.*, *Nature Nanotechnol* (2009) **4**, 861.
92. Bunch, J. S., *et al.*, *Nano Lett* (2008) **8**, 2458.
93. Frank, I. W., *et al.*, *J Vac Sci Technol B* (2007) **25**, 2558.
94. Cerda, E., and Mahadevan, L., *Phys Rev Lett* (2003) **90**, 074302.
95. Park, C. H., *et al.*, *Phys Rev Lett* (2008) **101**, 126804.
96. Park, C. H., *et al.*, *Nano Lett* (2008) **8**, 2920.
97. Park, C. H., *et al.*, *Nature Physics* (2008) **4**, 213.
98. Brey, L., and Fertig, H. A., *Phys Rev Lett* (2009) **103**, 046809.
99. Guinea, F., *et al.*, *Nat Phys* (2009) **6**, 30.
100. Levy, N., *et al.*, *Science* (2010) **329**, 544.